BIOCHEMISTRY
including biophysical chemistry & molecular biology
Article

Biochemistry **2009,** *48,* 5849–5863 5849
DOI: 10.1021/bi900235g

Conformational Dynamics of Metal-Binding Domains in Wilson Disease Protein: Molecular Insights into Selective Copper Transfer †

Agustina Rodriguez-Granillo,[‡] Alejandro Crespo,[§] and Pernilla Wittung-Stafshede*[,‡,∥]

[‡]*Department of Biochemistry and Cell Biology, Rice University, Houston, 77251 Texas,* [§]*Department of Bioengineering, Rice University, Houston, 77005 Texas, and* [∥]*Department of Chemistry, Umea University, 901 87 Umea, Sweden*

†*Funds were provided by the Robert A. Welch Foundation (C-1588) and the Swedish Research Council (2008-2947). Partial support comes from Rice Computational Research Cluster (NSF CNS-0421109), the Shared University Grid at Rice (NSF EIA-0216467), and from a partnership between Rice University, Sun Microsystems, and Sigma Solutions, Inc.*

Received February 13, 2009; Revised Manuscript Received May 16, 2009

ABSTRACT: ATP7A/B are human P_{1B}-type ATPases involved in cellular Cu homeostasis. The N-terminal parts of these multidomain proteins contain six metal-binding domains (MBDs) connected by linkers. The MBDs are similar in structure to each other and to the human copper chaperone Atox1, although their distinct roles in Cu transfer appear to vary. All domains have the ferredoxin-like fold and a solvent-exposed loop with a MXCXXC motif that can bind Cu^I. Here, we investigated the dynamic behavior of the individual MBDs (WD1−WD6) in ATP7B in apo forms using molecular dynamic simulations. We also performed simulations of three Cu-bound forms (WD2c, WD4c, and WD6c). Our results reveal molecular features that vary distinctly among the MBDs. Whereas WD1, WD2, and WD6 have well-defined Cu loop conformations stabilized by a network of interactions, WD4 and WD5 exhibit greater loop flexibility and, in WD4, helix α1 unwinds and rewinds. WD3, which has the lowest sequence identity, behaves differently and its Cu loop is rigid with respect to the rest of the domain. Cu coordination reduces structural dynamics in all domains but WD4c. In agreement with predictions on individual domains, simulations of the six possible Atox1−WD heterocomplexes show that Atox1 interactions with WD4 are the strongest. This study provides molecular explanations for reported Cu transfer and protein−protein interaction specificity.

Cellular copper (Cu)[1] homeostasis is maintained by highly regulated Cu-trafficking pathways (*1*, *2*), which result in undetectable amounts of free Cu (*3*). In humans, the Cu chaperone Atox1 (also referred in the literature as HAH1) binds and delivers Cu to two P_{1B}-type ATPases that couple ATP hydrolysis to Cu transport across membranes: the Menkes (or ATP7A) and Wilson (or ATP7B) disease proteins (*4*−*6*). Under normal conditions, these proteins are located in the membrane of the trans-Golgi network and deliver Cu to the secretory pathway for metalation of cuproenzymes, including ceruloplasmin (*2*). When the intracellular Cu concentration increases, ATP7A/B export excess Cu outside the cell (*2*). Mutations in these two proteins can result in severe human diseases, including Menkes and Wilson diseases (*7*).

ATP7A/B are multidomain proteins consisting of eight transmembrane domains, six N-terminal metal-binding domains (MBDs) termed MK*i* in ATP7A and WD*i* in ATP7B (where *i* is the number of the domain 1−6, with 1 being the most N-terminal domain), an actuator domain, and an ATP-binding domain that is composed of a phosphorylation subdomain and nucleotide-binding subdomain (*8*, *9*) (Figure 1). Solution structures of all apo and holo forms of MK1−MK6 (*10*−*15*) and apo forms of the WD34 (*16*) and WD56 (*17*) constructs have been published. Each ∼70 residue MBD has a ferredoxin-like fold with a compact $\beta\alpha\beta\beta\alpha\beta$ structure and a conserved metal-binding motif $MX_1CX_2X_3C$, located in the solvent-exposed $\beta1-\alpha1$ loop, which binds a single Cu^I ion (*18*, *19*) (Figure 1). The complete N terminus of ATP7B is about 630 residues long, which leaves about 200 residues in linker regions that connect the six domains. The linker lengths between the domains differ: the longest linker is 57 residues and situated between WD4 and WD5, whereas the shortest linker is 4 residues and situated between WD5 and WD6.

Structural work has demonstrated that Cu chaperones and target MBDs from various organisms possess the same fold and coordinate Cu^I via the two conserved Cys with a proposed S−Cu−S quasi-linear coordination geometry (*4*, *20*−*24*). All MBDs in ATP7A/B can bind Cu^I *in vitro* (*18*, *19*, *25*) with similar affinities (*26*, *27*). However, genetic and biochemical studies suggest that the MBDs are not functionally equivalent (*28*−*30*). For example, yeast two-hybrid assays suggest that the

*To whom correspondence should be addressed. Telephone: 46-90-786-5347. Fax: 46-90-786-7655. E-mail: pernilla.wittung@chem.umu.se.

[1]Abbreviations: Cu, copper; MBD, metal-binding domain; MK, Menkes disease protein MBD; WD, Wilson disease protein MBD; MD, molecular dynamics; rmsd, root-mean-square deviation; rmsf, root-mean-square fluctuation; vdW, van der Waals; HB, hydrogen bond.

Published on Web 05/18/2009

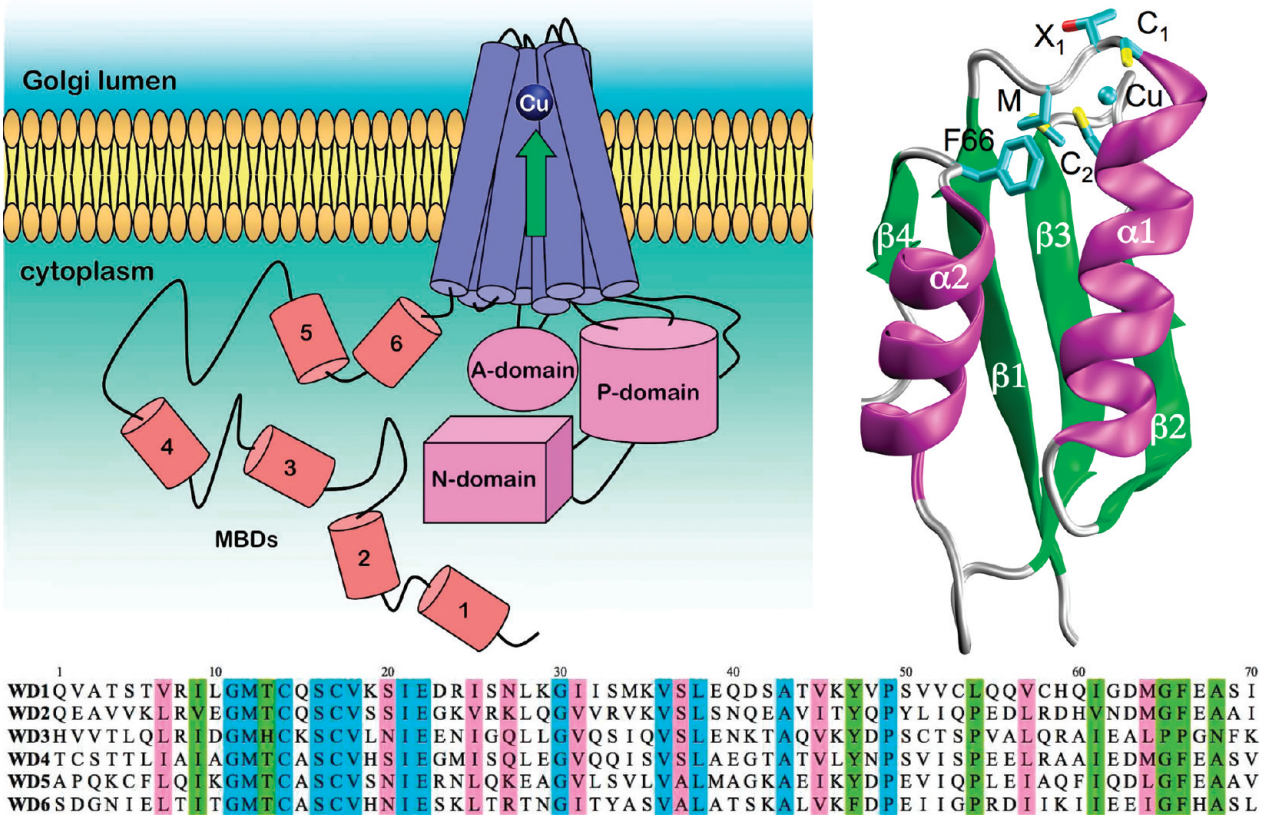

FIGURE 1: (Up, left) Schematic picture of ATP7A/B with its functional domains, including the actuator (A), phosphorylation (P), and nucleotide binding (N) domains and the MBDs. (Up, right) Structure of an individual MBD (holo-MK1, 1KVJ.pdb) revealing its ferredoxin-like fold. Residues M, X_1 (Thr/His), C_1, and C_2 from the conserved $MX_1C_1X_2X_3C_2$ motif and the conserved F and Cu are labeled. (Bottom) Multiple sequence alignment of WD1−WD6. Residues highlighted in blue are completely conserved; residues highlighted in green are conserved in all but one domain; and residues highlighted in pink are conserved in some but are similar.

interaction between Atox1 and MBD1−MBD4 is the strongest, whereas there is no interaction with MBD5 or MBD6 (*31*−*33*). In the case of ATP7A, NMR experiments suggest that both MK1 and MK4 can form a Cu-dependent complex with Atox1 (*12*, *34*). On the other hand, Cys-labeling studies (*23*) and NMR experiments (*16*, *17*) suggest that, in ATP7B, WD2 and WD4 can form a Cu-dependent adduct with Atox1, whereas WD56 can receive Cu not from Atox1 but from Cu-loaded WD4 (*17*). To gain insight into intrinsic structural and dynamic differences among individual WD domains that may serve as selectivity filters for Atox1 recognition and interdomain Cu transfer, we have performed molecular dynamics (MD) simulations of a set of WDs in the absence and presence of Cu. Our data reveal distinct molecular properties of the different domains that can be linked to variations in Atox1 and interdomain interactions. Furthermore, our predictions based on individual domains are validated by Atox1−WD heterocomplex simulations.

COMPUTATIONAL METHODS

Initial Structures. MD simulations were performed for apo forms of WD1, WD2, WD3, WD4, WD5, and WD6; WD2, WD4, and WD6 in Cu-loaded holo forms; and the six different Atox1−WD heterocomplexes, consisting of holo-Atox1 and each apo-WD. The initial structures for the apo forms correspond to the nuclear magnetic resonance (NMR)-reported Protein Data Bank (PDB) structures: WD34 (2ROP) (*16*) and WD56 (2EW9) (*17*). Apo-WD1 and WD2 structures were generated by homology-threading calculations with the program Modeler (*35*), using the structure of the WD56 construct as a template (2EW9.pdb, 36% sequence identity). For holo forms of WD2, WD4, and WD6, Cu^I was inserted between the Cys(S) atoms in structures obtained from the MD simulations of the corresponding apo forms (see below for details), where the S−S distance was lower than 5 Å. The initial structures for the six different heterocomplexes were generated using the final structures obtained from the MD simulations of the corresponding apo-WDs (see below for details) and the final structure obtained from our previously reported MD simulation of holo-Atox1 (*24*). The relative orientation of the chaperone and target domain in the complex was obtained by homology-threading calculations with the program Modeler (*35*), using the holo-Atox1 homodimer crystal structure (1FEE.pdb) as a reference (*36*).

MD Simulations. Simulations were performed for the different systems using Amber9 (*37*). The initial structures were immersed in a pre-equilibrated truncated octahedral cell of TIP3P explicit water molecules (*38*), and counterions were added to neutralize the systems (*37*). The coordinating Cys and Cu^I in the holo forms were parametrized as reported below. The rest of the protein atoms were described with the parm99SB force field parametrization (*39*). The protonation state of the titratable residues corresponds to the stable form at pH 7. Water molecules extended at least 10 Å from the surface of the proteins. Simulations were performed in the NPT ensemble (constant pressure of 1 atm and temperature of 300 K was maintained using the Berendsen coupling scheme (*40*)), employing periodic boundary conditions. A SHAKE algorithm was employed to keep bonds involving hydrogen atoms at their equilibrium length (*41*). The systems were optimized and equilibrated for 200 ps at 300 K. The

Table 1: Total Simulation Time, Backbone rmsd for the Entire Simulation ($rmsd_{total}$, with Respect to the First Structure) and for the Last 100 ns of the Simulation ($rmsd_{100}$, with Respect to the Average Structure), and Backbone rmsd between the Initial and Last Structures from the Entire Simulations (Δrmsd)

	time (ns)	$rmsd_{total}$ (Å)	$rmsd_{100}$ (Å)	Δrmsd (Å)
WD1	143	1.9 ± 0.2	1.1 ± 0.2	1.5
WD2	133	1.6 ± 0.3	1.2 ± 0.3	1.2
WD3	116	1.7 ± 0.3	1.1 ± 0.3	2.0
WD4	132	2.1 ± 0.3	1.4 ± 0.2	1.5
WD5	140	3.6 ± 0.2	1.3 ± 0.4	3.3
WD6	125	1.8 ± 0.2	0.9 ± 0.2	2.1
WD2c	126	1.4 ± 0.1	0.9 ± 0.2	1.2
WD4c	135	2.5 ± 0.2	1.3 ± 0.3	2.2
WD6c	127	1.0 ± 0.2	0.8 ± 0.2	0.7

structures were then simulated until the root-mean-square deviation (rmsd) as a function of time was stable for 100 ns (for individual WDs, see Table 1) and 10 ns (for the holo-Atox1−WD heterocomplexes; total simulation time was ~35 ns for each). The converged last 100 or 10 ns were used for data analysis. rmsd, rms fluctuations (rmsf) per residue, and protein/solvent radial distribution functions $g(r)$ were calculated for each of the systems using the ptraj module of Amber9 (*37*). The electrostatic potential for each system was calculated using the APBS program (*42*).

Cu Center Parametrization. To perform the simulations of holo-WD2, holo-WD4, and holo-WD6, we employed the same parametrization for the Cu^I center in all systems. As opposed to conventional QM vacuum parametrizations, we decided to perform QM−MM geometry optimizations of the three holo-WDs to include the effects of the protein and solvent environments in the calculation. We have previously shown that, in a related Cu chaperone, the environment significantly affects the geometrical and electronic parameters of the Cu^I center, in comparison to a sole QM optimization in vacuum of a Cu^I atom plus two methythiolate groups (*30*).

Starting from the generated holo forms of WD2, WD4, and WD6 (see before), we first performed short classical MD simulations using Amber9 (*37*) to relax and equilibrate these initial structures. The solvated structures were optimized and then equilibrated by performing 700 ps of classical MD simulations at 300 K, followed by a simulated annealing calculation (200 ps), in which the temperature was slowly decreased to 0 K. In these short simulations, the parameters for the Cu^I center were taken from a previous calculation of a Cu^I chaperone that shares a similar Cu^I coordination motif (*24*). The parameters for the remaining atoms and the simulation details are the same as described in the preceding MD section. The annealed structures were subsequently optimized with a QM−MM implementation (*43*) of the SIESTA code (*44*), in which the QM subsystem (Cu^I atom plus two methylthiolate groups) is treated at the density functional theory (DFT) level. For the past decade, DFT has been the first method of choice to perform electronic structure calculations of biological systems, particularly for systems that include transition-metal atoms (*45*). For all atoms, basis sets of double-ξ plus polarization quality were employed, with a pseudo-atomic orbital energy shift of 25 meV and a grid cutoff of 150 Ry (*44*). All calculations were performed with the spin-unrestricted approximation using the generalized gradient approximation functional proposed by Perdew et al. (*46*). This combination of functional, basis sets, and grid parameters has been previously validated for similar molecular systems that include Cu atoms (*24*, *45*).

The equilibrium parameters for the Cu^I center employed in the MD simulations on the holo forms (see the preceding MD Simulations section) were therefore taken as the average value of the QM−MM optimized Cu forms of WD2, WD4, and WD6 structures (Cu−S = 2.154 Å; S−Cu−S = 158.2°; and C−S−Cu = 101.1°). The atomic charges for Cu^I coordinated to two methylthiolate groups were determined using restricted electrostatic potential (RESP) (*47*) and HF/6-31G(d) single-point wave functions over the QM−MM optimized structures, with Gaussian 03, revision D.01 (*48*), following the protocol recommended in the Amber web page (amber.scripps.edu). The atomic charges employed in the MD simulations also correspond to the averaged RESP charges over the QM atoms together with the charges of an Amber classical cysteinate residue (CYM) modified to maintain an overall integer charge of −1 (qCu^I = 0.388 252 e, and qS = −0.730 695 e). The van der Waals (vdW) parameters for Cu^I were taken from ref (*49*), and the bond and angle force constants involving the Cu^I atom were taken from ref (*50*). This combination of parameters is similar to those previously reported (*24*, *49*). Finally, for the heterocomplex simulations, the parameters of the coordinating Cys and Cu^I in holo-Atox1 were taken from ref (*24*).

Free Energy Calculations. Atox1−WD binding free energies (ΔG) for the six different heterocomplexes were estimated using the sietraj program (*51*). This program calculates ΔG for snapshot structures from the MD simulations as the sum of the intermolecular vdW and Coulomb interactions plus the change in reaction field energy (determined by solving Poisson−Boltzmann equation) and nonpolar solvation energy (proportional to the solvent-accessible surface area). ΔG is then scaled by an empirically determined factor (*51*). Here, we estimated ΔG by averaging 100 calculations from the last 10 ns of the MD simulations of the heterocomplexes.

RESULTS

We have performed MD simulations of the six individual WDs (WD1−WD6) of ATP7B. To investigate the effect of Cu coordination in individual domains, we further simulated holo-WD2 (WD2c), holo-WD4 (WD4c), and holo-WD6 (WD6c). These three holo domains were selected, because available data (at the time of this study) suggested that these domains preferably form Cu-dependent adducts with Atox1 (in the case of WD2 and WD4) and with WD4 (in the case of WD6). Below, we first report our computational findings for (1) individual apo domains, grouped based on behavior, followed by (2) the individual holo domains. Finally (3), we report on an analysis of protein−protein interactions as well as free energy of binding in the six different Atox1−WD heterocomplexes.

1. Apo Forms of WD1−WD6. Apo forms of WD1, WD2, WD3, WD4, WD5, and WD6 were subjected to MD simulations for more than 100 ns each. The backbone rmsd (with respect to the first structure) show that WD5 undergoes the largest conformational change during the entire simulation (Figure 2A and Table 1). In the last 100 ns, which were used for data analysis, the rmsd (with respect to the average structure) suggest no significant conformational changes in any of the apo domains (Table 1).

Backbone fluctuations of WD4 and WD5 are similar, and the Cu loop and helix α1 are significantly more flexible (except for

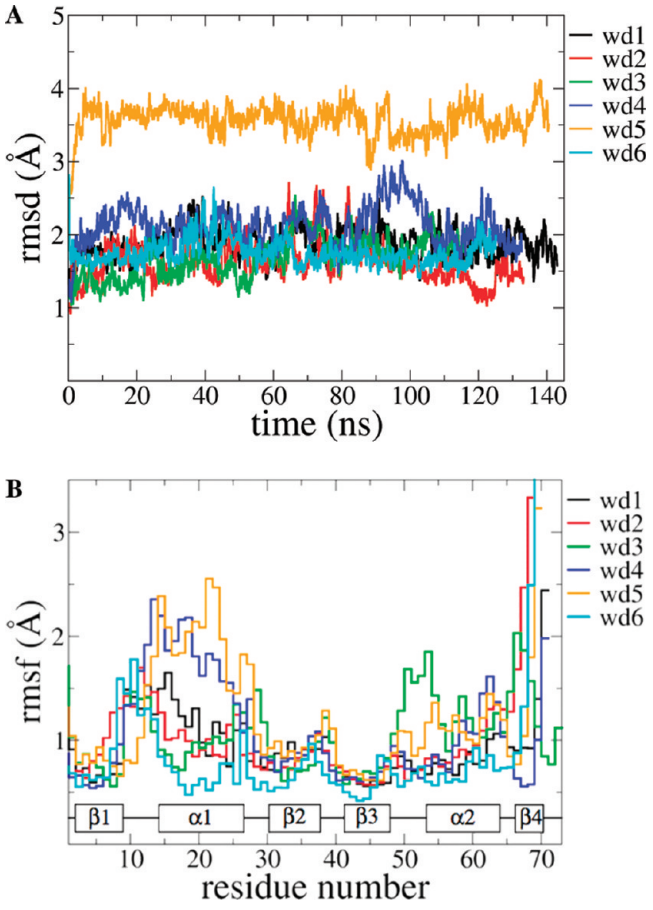

FIGURE 2: (A) rmsd (in angstroms, with respect to the first structure) of the backbone heavy atoms (N, C_α, and C) as a function of simulation time for the apo domains. (B) Average fluctuations (rmsf in angstroms) of backbone heavy atoms (N, C_α, and C) per residue for the apo domains. The secondary structure elements are shown (reference is WD1 final structure). Black, WD1; red, WD2; green, WD3; blue, WD4; orange, WD5; cyan, WD6.

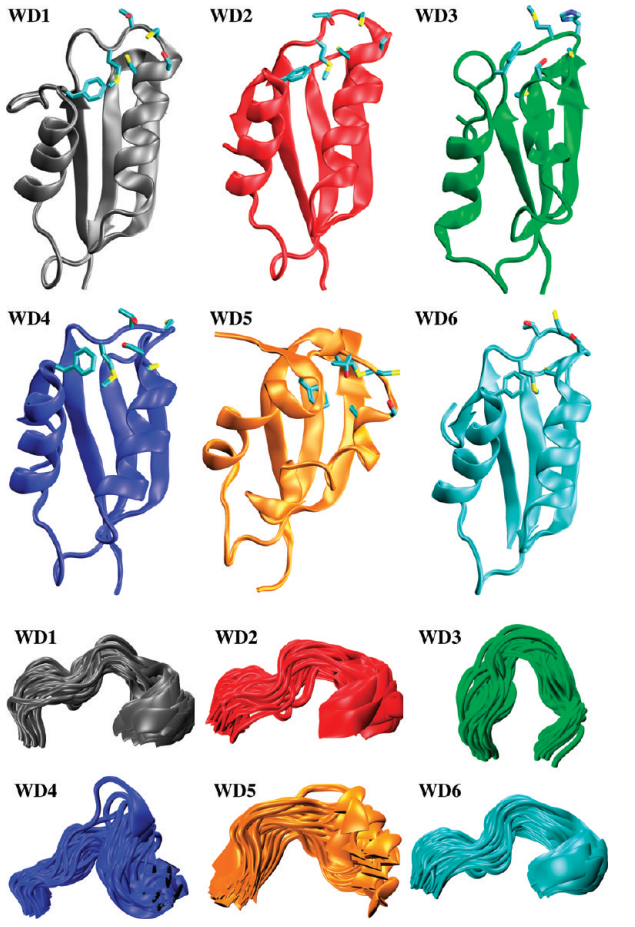

FIGURE 3: (Top) Final structures of WD1 (black), WD2 (red), WD3 (green), WD4 (blue), WD5 (orange), and WD6 (cyan) in the apo forms. For each domain, residues M, X_1, C_1, and C_2 from the conserved $MX_1C_1X_2X_3C_2$ motif and the conserved Phe are shown. (Bottom) 50 representative conformations of the Cu loop in the production run for the apo domains.

the C-terminal ends) than the other domains (Figure 2B). The trend in fluctuations in WD4 and WD5 is similar to that found for the bacterial Cu chaperone CopZ (*24*). The fluctuations found in WD1, WD2, and WD6 are similar to each other and differ from those of WD4 and WD5 (Figure 2B); although the Cu loops are more flexible than the rest of the domains (excluding C-terminal ends), they are much less floppy in these three domains than observed in WD4 and WD5 Cu loops. WD6 is the least floppy of the six WD domains studied; its fluctuation pattern is similar to that found earlier in the human Cu chaperone Atox1 (*24*). Backbone fluctuations in WD3 do not correspond to either of the mentioned groups. This protein appears rigid in the Cu loop but more flexible in $\beta3-\alpha2$ and $\alpha2-\beta4$ loops.

1.1. Apo Forms of WD1, WD2, and WD6: Stable Domains with Well-Defined Cu Loops. The final structures of WD1, WD2, and WD6 after the simulations are similar to each other, typical of a well-packed ferredoxin-like fold (Figure 3 and Table 2), and do not differ significantly from the starting structures (Table 1). The secondary-structure elements are well-defined, helices α1 and α2 are parallel and properly packed against the β sheet. Also, the conformation of key residues around the Cu loop is very similar, including the Cu binding Cys, the conserved Met, residues X_1 and X_3, and the conserved Phe located in the $\alpha2-\beta4$ loop. The final structures of WD1, WD2, and WD6 are also very similar to that of Atox1 (*24*). The dynamics of helix α1 in WD1, WD2, and WD6 changes throughout the production MD simulation; although it does not unwind completely, the beginning of this helix loosens up (opens up) and returns to the original conformation several times (Figure 3). This movement is subtler in WD6, in which helix α1 appears more rigid.

Table 2: rmsd (in Angstroms) between the Corresponding Final Structures

	WD1	WD2	WD3	WD4	WD5	WD6	WD2c	WD4c	WD6c
WD1	0	1.5	2.3	1.9	3.1	1.4			
WD2		0	2.4	1.5	2.6	1.4	1.1		
WD3			0	2.6	2.9	2.3			
WD4				0	2.1	1.5		1.7	
WD5					0	2.6			
WD6						0			1.4
WD2c							0	1.7	1.0
WD4c								0	1.7
WD6c									0

Consistent with similar fluctuations and structures observed for WD1, WD2, and WD6, all of them exhibit similar interactions involving the Cu loop residues (Figure 4). Both Cu-binding Cys side chains are flexible and move around freely during the simulations. The first Cys (Cys1) adopts two main conformations during the simulation, in which it interacts with either residue X_1 (Thr in these cases) or residue X_3 (Ser in all cases) (panels A and B of Figure 4). The second Cys (Cys2) also interacts with the Ser,

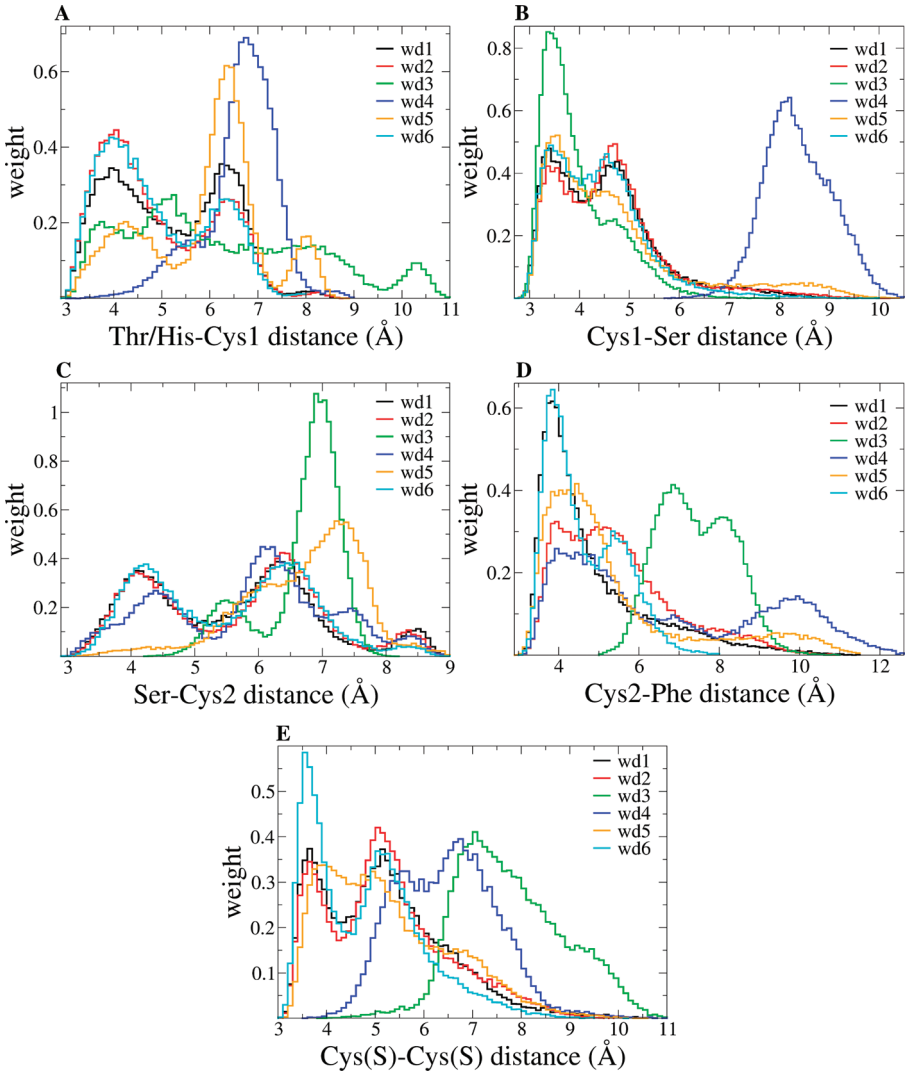

FIGURE 4: Histograms of distance distribution (in angstroms) between heavy atoms of (A) residue X_1 Thr/His (OG1/NE2) and Cys1 (SG), (B) Cys1 (SG) and residue X_3 Ser (OG), (C) residue X_3 Ser (OG) and Cys2 (SG), (D) Cys2 (SG) and Phe (CZ), and (E) Cys1 (SG) and Cys2 (SG) for the apo domains. Black, WD1; red, WD2; green, WD3; blue, WD4; orange, WD5; cyan, WD6.

although the interaction is weaker (Figure 4C), and with the Phe (Figure 4D). In contrast, the conserved Met is buried in the cores of all three domains (Figure 5A), and this side chain makes several contacts with residues in the $\beta2-\beta3$ sheet and residues close to the Cu loop (Phe and Cys2), which appears to stabilize the protein core. The terminal methyl of the Met (CE) interacts most of the simulation time with residues in the $\beta2-\beta3$ sheet, including the side chain of Val36 and Leu38 (numbering corresponds to WD1), which are conserved in all of the MBDs, the backbone of Gly41 and Ser42 in WD1 (Gln42 and Glu43 in WD2 and Ser39 and Lys40 in WD6), and Val18 (highly conserved among the MBDs, Figure 1) in helix α1. Moreover, the rest of the Met side chain (CB, CG, and SD) interacts with the Phe ring and Cys2.

The Cys residues are equally exposed to solvent in WD1, WD2, and WD6, but Cys1 is always more exposed than Cys2 (panels B and C of Figure 5). The S−S distance distribution between the Cu-binding Cys is also similar between these three domains and consists of two peaks centered at ~3.5 and ~5 Å (Figure 4E). These small distances allow for strong interactions between the residues. However, the weights of the S−S distance distribution peaks differ: the short distance is favored in WD6, but the longer distance is favored in WD2. Overall, in all of WD1, WD2, and WD6, the conserved residues Met, Thr, Ser, and Phe form a stable network of interactions with the Cu-binding Cys, which results in a Cu loop conformation that is relatively well-defined. This in turn seems to maintain the Cys side chains exposed to the solvent and in proximity to each other.

1.2. Apo Form of WD3: Most Divergent Domain of the Six. Among the six WDs, WD3 has the lowest sequence identity (Figure 1); therefore, it may not be surprising that this domain exhibits unique structural dynamics. Sequence differences around the Cu loop are residue X_1, which is a His in WD3 instead of a Thr, and position 66 in the multiple sequence alignment in Figure 1. Residue 66 is an invariant Phe in all MBDs, except in WD3 and MK3, where it is a Pro. However, WD3 contains a Phe located three positions downstream, which is also close to the Cu loop in the folded 3D structure (Figure 3). Therefore, this Phe in WD3 may have a similar role to the Phe in position 66 in the other domains.

The WD3 final structure after the simulation differs by more than 2 Å in rmsd with all of the other structures; WD1 and WD6 are the closest matches; and WD5 is the most different one (Table 2). The rmsf as a function of the residue is unique in WD3; the fluctuations are homogeneous throughout the sequence, and thus, the Cu loop is not more floppy than other regions

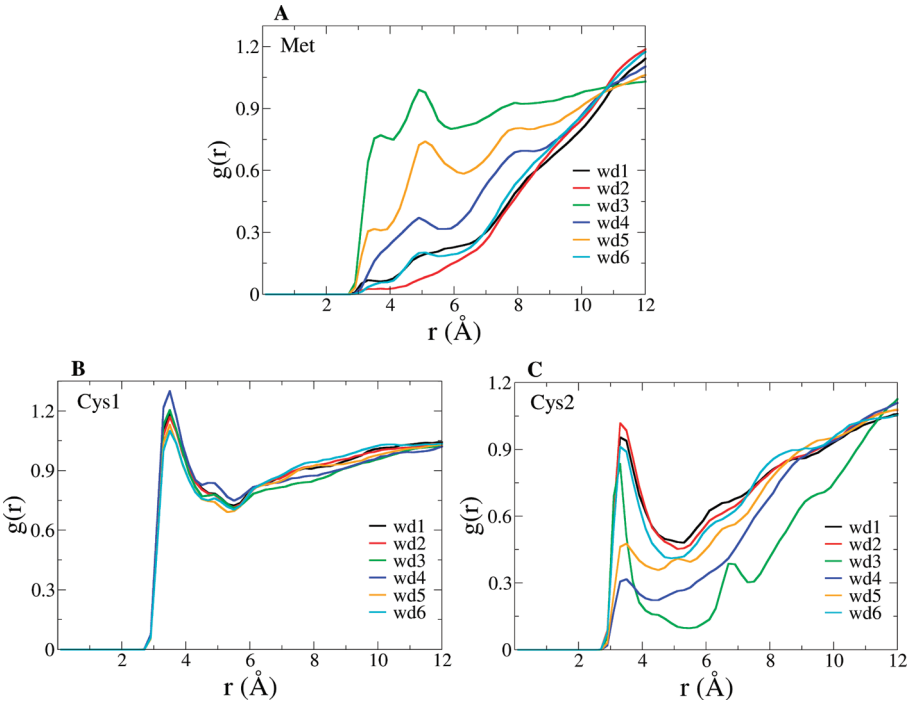

FIGURE 5: Protein−solvent radial distribution functions $g(r)$ of the S atoms of (A) Met, (B) Cys1, and (C) Cys2 for the apo domains. Black, WD1; red, WD2; green, WD3; blue, WD4; orange, WD5; cyan, WD6.

(Figure 2B). Particular flexibility (larger than in the Cu loop) is seen in helix α2, which is shorter than in the rest of the domains (because of the presence of two unique Pro at its C terminus), and the β3−α2 and α2−β4 loops. Helix α1 in WD3 is shorter at the C terminus, resulting in a longer α1−β2 loop (Figure 3). Also, because of the unique position of the Phe that, although further away in sequence, still interacts with the Cu loop, the α2−β4 loop is close to the N terminus of helix α1, as opposed to the other domains.

The interactions around the Cu loop are altered in WD3 as compared to WD1, WD2, and WD6 (Figure 4). Instead of interacting alternately with residues X_1 and X_3, as in the aforementioned domains, in WD3, Cys1 is exposed to the solvent (Figure 5B) and interacts only with residue X_3 (panels A and B of Figure 4), and both of these residues are in close contact with the Phe ring. These interactions seem to stabilize the Cu loop. In WD1, WD2, and WD6, interactions of Cys2 with the Ser and Phe maintain the Cys side chain solvent-exposed and close to the other Cys. In WD3, on the other hand, Cys2 is more buried (Figure 5C) and, consequently, does not interact with either Ser or Phe (panels C and D of Figure 4). Instead, it points to the hydrophobic core and interacts with Val18 in helix α1 and with Val36 and Leu38 in the β2 strand. Because of the interactions described above, the Cys−Cys distance distribution differs with respect to the other domains, with a peak centered at ∼7 Å (Figure 4E). The conserved Met is completely solvent-exposed in WD3 (Figures 3 and 5A). This does not correlate with increased backbone fluctuations in the Cu loop because (a) the interface formed by Cys1, Ser, and Phe stabilizes the Cu loop and restricts the motion of Met, (b) Cys2 provides many core contacts that in WD1, WD2, and WD6 are provided by their buried Met, and (c) the Met side chain interacts with residue X_1 (His) and Lys41 in the β2−β3 loop.

1.3. Apo Forms of WD4 and WD5: Flexible Domains with Large Changes in Helix α1. WD4 and WD5 exhibit similar fluctuations to each other during the simulation, with helix α1 observed as a particularly floppy region (Figure 2B). A comparison of the final structures reveals that WD4 is most similar to WD2 and WD6, and it differs the most with the WD3 structure (Table 2). The final structure of WD4 does not differ much from the initial structure (Table 1), and the Cu loop appears well-organized, as also found in WD1, WD2, and WD6 (Figure 3). However, helix α1 and the last part of the Cu loop in WD4 present unique dynamics that is absent in the other domains. Residues 19 (which corresponds to Cys2) to 24 at the N terminus of helix α1 of WD4 completely unwind and rewind during the simulation. This unique unwinding/rewinding process distinguishes WD4 from the other domains in the N terminus of ATP7B.

Because of the dynamics of helix α1, the interactions around the Cu loop are weaker in WD4 (Figure 4). However, at the times when this helix is folded, several interactions maintain a well-organized Cu loop. The Phe side chain is buried and interacts with Met, Ser, and Cys2, which stabilizes the Cu loop. The conserved Met is buried but not to the same extent as noted in WD1, WD2, and WD6 (Figure 5A): it is flexible; during the first ∼70 ns of simulation, it interacts with Leu40 and Gly43 in the β2−β3 loop; and in the last ∼30 ns, it moves deeper inside toward the β2−β3 sheet. When all domains studied are compared, Cys1 is most exposed in WD4 (Figure 5B) and does not interact with Thr or Ser (panels A and B of Figure 4); instead, it interacts with Leu40 in the β2−β3 loop. On the other hand, Cys2 in WD4 is buried (Figure 5C) and makes contacts with several residues, including Ser and Phe (panels C and D of Figure 4), Val20 in helix α1, Val38 in strand β2, and Leu40. The Cys−Cys distance distribution in WD4 consists of two peaks centered at ∼5.5 and ∼7 Å, which differs significantly from that found for WD1, WD2, WD5, and WD6 (Figure 4E). Notably, the Cys−Cys distances found here for WD4 are similar to those previously observed for the apo form of Atox1 (*24*).

The WD5 final structure after the simulation differs significantly from the starting point structure (Table 1). It also differs

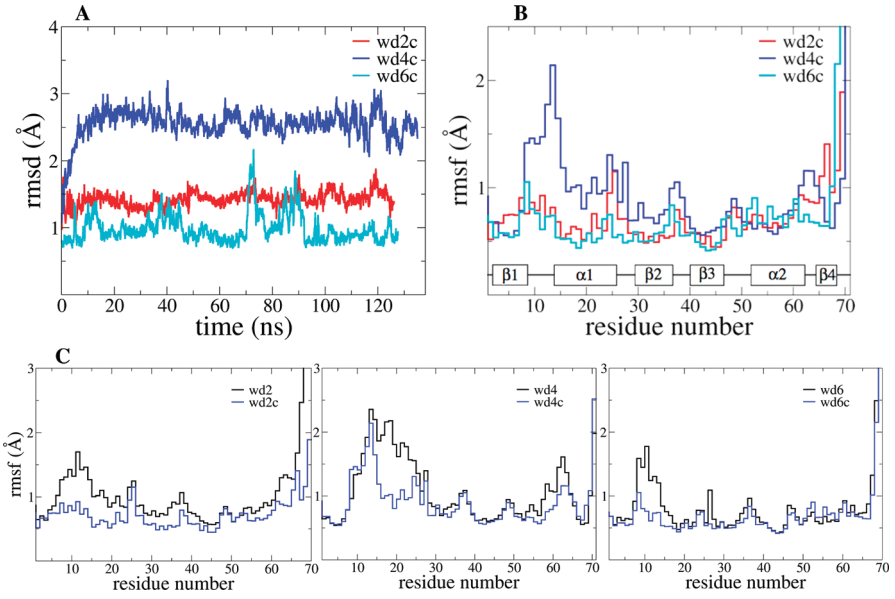

FIGURE 6: (A) rmsd (in angstroms, with respect to the first structure) of the backbone heavy atoms (N, C_α, and C) as a function of the simulation time for the holo domains. (B) Average fluctuations (rmsf in angstroms) of backbone heavy atoms (N, C_α, and C) per residue for the holo domains. The secondary-structure elements are shown (reference is WD1 final structure). Red, WD2c; blue, WD4c; cyan, WD6c. (C) Comparison of rmsf between apo (black) and holo (blue) forms of WD2, WD4, and WD6.

more than 2 Å in rmsd with the rest of the structures, with WD4 being the closest match and WD1 being most different (Table 2 and Figure 3). Helix α1 has increased flexibility in WD5: it loses secondary structure and becomes distorted during the simulation. As opposed to WD4, in which helix α1 unwinds and rewinds, in WD5, helix α1 does not return to the original conformation during the entire 140 ns run. Moreover, because of the unwinding and bending of this helix, interactions with strand β2 are lost, and this interface is therefore significantly weakened. Also, the orientation of helices α1 and α2 with respect to the antiparallel β sheet changes. The bending and altered orientation occur because (a) strand β1 is extended and, as a result, the Cu loop is shorter and the conserved Met is no longer part of the loop and (b) the conserved Phe, which is located in strand β4 in this domain, is completely buried in the core.

In WD5, the Cu loop is particularly short (only four residues; Figure 3) and only some of the interactions around the active site seen in the other domains are conserved (Figure 4). The Met side chain interacts most of the time with Val37, Leu 39 in strand β1, and the Phe (which is completely buried). However, the destabilization of helix α1 and strand β2 interface allows for interactions between the Met side chain and the solvent (Figure 5A). Similar to the other domains, Cys1 is exposed (Figure 5B) and interacts with Ser (panels A and B of Figure 4). Because of the unusual proximity between the Cu and α2−β4 loops in WD5, the conserved Thr interacts with Gly66. Cys2 is more buried than Cys1 (Figure 5C) and adopts two major conformations: it points to the core and interacts with Phe, or it interacts with Cys1 (panels D and E of Figure 4). As a result, the Cys−Cys distance distribution in WD5 consists of two peaks, both centered at short distances of ~4 and ~5 Å.

2. Holo Forms of WD2, WD4, and WD6. WD2c, WD4c, and WD6c were simulated for more than 100 ns, and the backbone rmsd (with respect to the first structure) in the entire simulation indicates that WD4c is the domain that undergoes the largest conformational change (Figure 6A and Table 1). In the last 100 ns of the simulation, all of the domains are stable and exhibit small fluctuations with respect to the corresponding apo forms (Table 1). Backbone fluctuations of WD2c and WD6c are similar (Figure 6B) and comparable to those observed previously for holo-Atox1 (*24*). Interestingly, in WD4c, the Cu loop is more flexible than the rest of the protein, even more floppy than observed in the same region in apo forms of WD1, WD2, and WD6. Nevertheless, in all cases, including WD4c, Cu coordination reduces the overall backbone fluctuations (Figure 6C).

Table 3: rmsd (in Angstroms) between the Holo-WD (Initial and Final) and the Corresponding Holo-MK Structures: MBD2c (WD2c versus 1S6U.pdb, Ref (*11*)), MBD4c (WD4c versus 2AW0.pdb, Ref (*10*)), and MBD6c (WD6c versus 1YJV.pdb, Ref (*13*))

	initial	final
MBD2c	1.5	1.6
MBD4c	1.7	1.8
MBD6c	1.2	1.1

To validate our generated holo structures, we compared them to the corresponding holo domains of ATP7A, for which NMR solution structures are available (the structure of MK4 was solved in the presence of Ag^I, which has similar coordination chemistry to Cu^I) (*10*, *11*, *13*). Our three holo structures are between 1.1 and 1.8 Å from the corresponding NMR structures of MKs (Table 3), validating our structures. Moreover, if we compare our QM−MM optimized structures with the corresponding NMR structures, the geometry of the active site is similar in all cases. WD2c optimized with a S−Cu−S angle of 156.1° versus 140 ± 40° found for MK2c (*11*). WD4c optimized with a geometry in which the S atoms of the two Cys are separated by 4.31 Å, similar to the 4.8 ± 0.2 Å in Ag^I-loaded MK4 (*10*). In the case of WD6c, it also optimized with a S−S distance of 4.31 Å, which is close to an average of 4.27 ± 0.03 Å in MK6c (*13*).

The final structures of WD2c and WD6c are very similar to each other, with rmsd of only 1.0 Å (Table 2 and Figure 7). However, the WD4c final structure differs 1.7 Å with the other holo structures (Table 2 and Figure 7). The conformation of key residues around the Cu loop is very similar in WD2c and WD6c,

and this conformation matches that found for holo-Atox1 (*24*). The structure of WD4c differs from the other holo proteins mainly in the Cu loop and the beginning of helix α1. In WD4c, the Cu loop is longer: eight residues (including Cys2) in WD4c versus four and five residues in WD2c and WD6c, respectively (Figure 7). This means that the N-terminal end of helix α1 unwinds and both Cys are located in the Cu loop in WD4c, which may explain the observed higher fluctuations in this region (Figure 6B). This structural change exposes the Cu bis-thiolate center in WD4c to the solvent as opposed to the other holo domains.

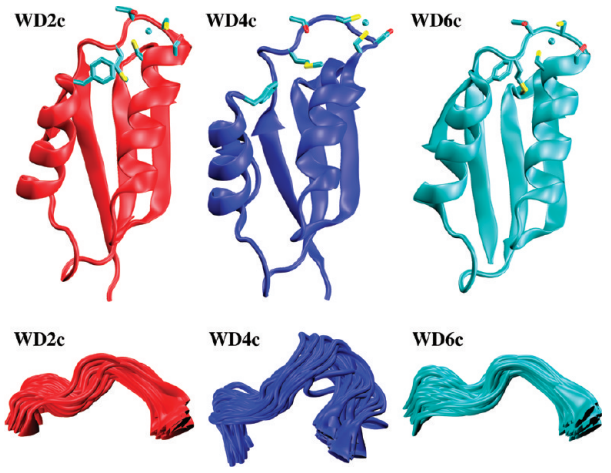

FIGURE 7: (Top) Final structures of WD2c (red), WD4c (blue), and WD6c (cyan) in the holo forms. For each domain, the Cu atom and residues M, X_1, C_1, and C_2 from the conserved $MX_1C_1X_2X_3C_2$ motif and the conserved Phe are shown. (Bottom) 50 representative conformations of the Cu loop in the production run for the holo domains.

The interactions around the Cu center are similar between WD2c and WD6c (Figures 7 and 8). The conserved Thr and Ser side chains interact extensively with Cys1 (panels A and B of Figure 8), which provides electrostatic stabilization to the Cu center. The Phe side chain remains close to the Cu loop and interacts with Cys2 (Figure 8D), which further stabilizes the Cu site. Moreover, Cys1 and Cys2 form a hydrogen bond (HB) with the backbone amide of Ser and Thr, respectively. The Met side chain is completely buried in WD2c and WD6c holo domains (Figure 9A), like in the apo forms, and interacts with residues in the $\beta2-\beta3$ sheet, Phe, and Cys2. Altogether, this extensive network of interactions appears to maintain stable and rigid structures of these two holo domains. In both domains, Cys1 is exposed to the same extent (Figure 9B), because it has a similar conformation in both structures. However, Cys2 is more buried in WD6c (Figure 9C), because, in contrast to WD2c, it points toward the loop backbone.

In contrast, most of the mentioned interactions around the Cu loop are absent in WD4c (Figures 7 and 8). The dynamics of Met in WD4c changes throughout the simulation: during the first ~80 ns, it interacts with Ile11 in strand $\beta1$, Leu40 and Val38 in $\beta2$, and with the Phe ring, but in the last ~20 ns, this side chain points to the Cu loop, where it becomes exposed to the solvent (Figures 7 and 9A). This may also contribute to an increase in the fluctuations of the Cu loop. Furthermore, the Phe side chain does not interact with Cys2 (Figure 8D) but with the hydrophobic core. This is mainly due to the conformation of the loop, which is protruding from the surface of the protein and too far away for Phe to reach to it (Figure 7). Therefore, the Cu bis-thiolate center is more exposed in WD4c, as shown by a marked increase in solvent exposure of Cys2 (Figure 9C). The Cu site is only stabilized by Ser, which interacts with both Cys residues (panels B and C of Figure 8), but the Thr remains far from the Cu center (Figure 8A). Overall, it emerges that the Cu is more exposed and

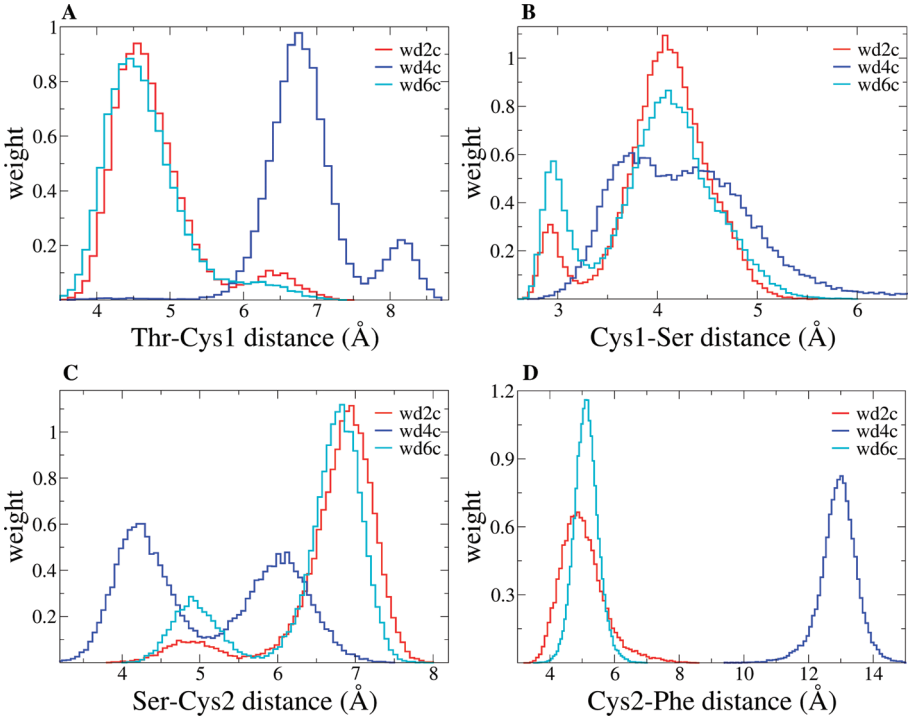

FIGURE 8: Histograms of distance distribution (in angstroms) between heavy atoms of (A) residue X_1 Thr (OG1) and Cys1 (SG), (B) Cys1 (SG) and residue X_3 Ser (OG), (C) residue X_3 Ser (OG) and Cys2 (SG), and (D) Cys2 (SG) and Phe (CZ), for the holo domains. Red, WD2c; blue, WD4c; cyan, WD6c.

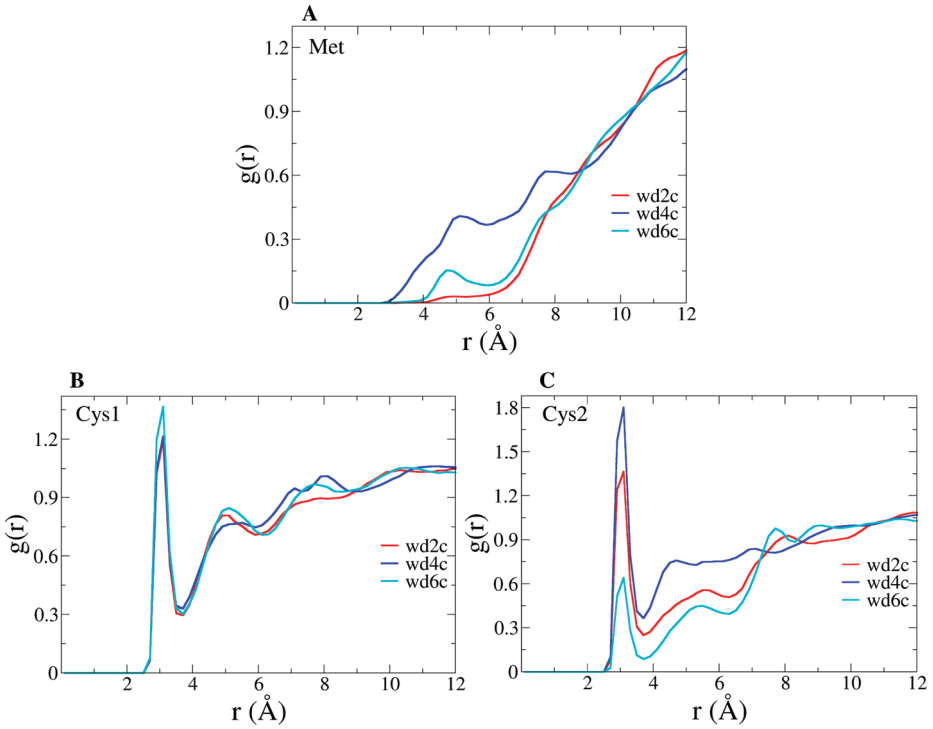

FIGURE 9: Protein−solvent radial distribution functions $g(r)$ of the S atoms of (A) Met, (B) Cys1, and (C) Cys2 for the holo domains. Red, WD2c; blue, WD4c; cyan, WD6c.

less protected in WD4c as compared to the other holo domains studied.

3. Protein−Protein Interactions in Atox1−WD Heterocomplexes. 3.1. Surface Electrostatic Analysis of Individual WDs. To address the involvement of electrostatic attraction in Atox1−WD and WD−WD interactions, we calculated the electrostatic surface potentials at the end of the simulations for all of the domains (apo and holo forms) (Figure 10). For comparison, we also performed this calculation for holo-Atox1 (using the structure at the end of our previous simulation) (*24*). The structures in Figure 10 have the same orientation as that in Figures 3 and 7, which shows the protein side in which chaperone and target domains are believed to interact (*16*, *17*, *34*, *52*). The surface charge distribution in Atox1 is mainly positive (Figure 10), because of the presence of one Arg and Lys in helix α1 and three Lys in helix α2. On the other hand, WD2 (apo and holo), WD4 (apo and holo), and WD5 have significant patches of negative surfaces, complementary to the positive ones of holo-Atox1. Whereas the WD2 and WD5 structures are mainly negative in helix α2 and the α2−β4 loop, most of the WD4 surface is negative, including helices α1 and α2 and the α2−β4 loop. These are the regions believed to form the chaperone−target adduct interface (*16*, *17*, *34*, *52*). WD1 has also patches of negative surface, although not as much as WD2, WD4, and WD5. On the other hand, WD3 and WD6 (apo and holo) have mainly positive charge distribution on this side.

3.2. Heterocomplexes between Holo-Atox1 and WDs. On the basis of our electrostatic analysis, we decided to perform a more quantitative analysis of Atox1−WDs interactions. For that, we generated the six different holo-Atox1−WD heterocomplexes using the orientation found in the Atox1 homodimer crystal structure and subjected these heterocomplexes to MD simulations (see Computational Methods). According to NMR data (*16*, *17*, *34*, *52*), these are the contact regions in the chaperone−target adduct.

Results from the heterocomplex MD simulations show significant as well as subtle differences among the six WDs. All Atox1−WD heterocomplexes, except for Atox1−WD3, were stable during the simulation time and maintained a similar conformation (see Figure 11A for the Atox1−WD4 final structure). On the other hand, the Atox1−WD3 heterocomplex was unstable and floppy, and after ∼10 ns, the interacting surface weakens and the complex adopts a different conformation, in which both proteins are further apart from each other. Finally, after ∼25 ns, the heterocomplex falls apart completely.

To quantify the strength of the protein−protein interactions, we calculated the ΔG of heterocomplex formation (see Computational Methods and Table 4). This analysis shows that WD4 is the WD that binds strongest to holo-Atox1 with $\Delta G = -9.5 \pm 0.4$ kcal/mol, whereas WD3 binds the weakest with $\Delta G = -4.2 \pm 0.6$ kcal/mol (value calculated before the complex falls apart). The second best holo-Atox1 binder is WD5, followed by WD2, WD1, and WD6, which all have similar ΔG values (Table 4). The intermolecular vdW interactions that contribute to the calculated ΔG are in the range from −45 to −50 kcal/mol in the different heterocomplexes, except in the Atox1−WD3 complex, in which it is −12 kcal/mol (Table 4). On the other hand, the electrostatic contributions differ among the heterocomplexes (Table 4). The Atox1−WD4 heterocomplex has the greatest intermolecular electrostatic interaction equal to ∼−170 kcal/mol, which is also accompanied with the greatest penalty of charge burial (change in reaction field energy; Table 4). The second strongest intermolecular Coulomb interactions are found in the WD5 heterocomplex, followed by WD2, WD1, WD6, and WD3 (Table 4). These results are completely consistent with and provide a quantitative interpretation of the surface electrostatic potential calculations of the individual domains described in the previous section. Finally, the last contribution to the calculated ΔG is the change in nonpolar solvation energy, which

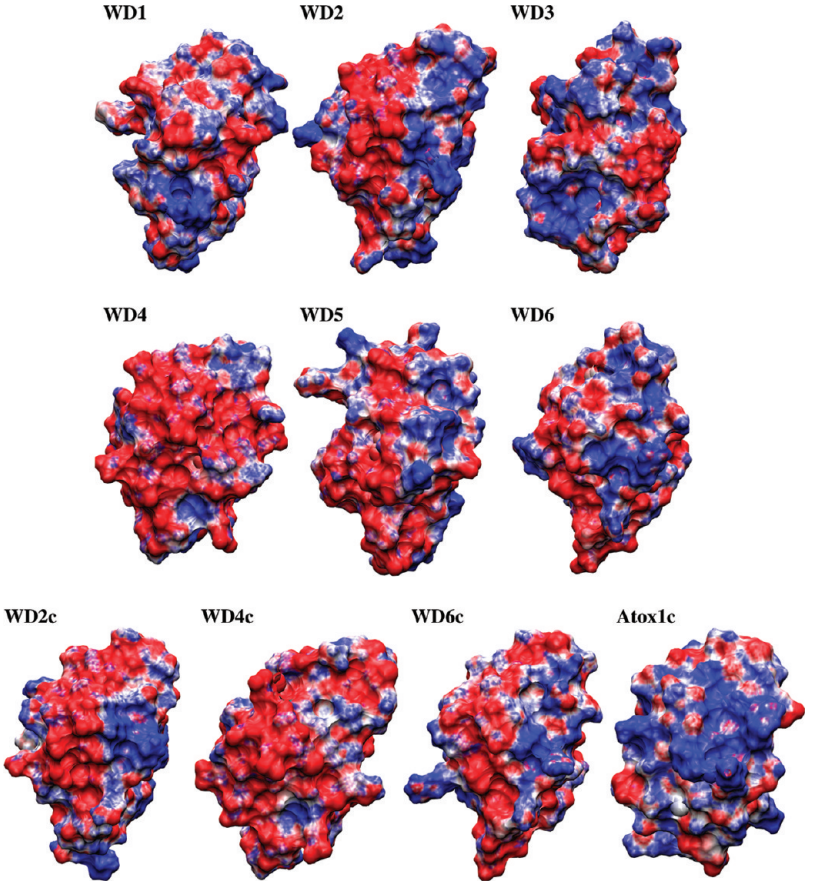

FIGURE 10: Comparison of the surface electrostatic potential of the apo (top) and holo (bottom) domains, using the final structures from the simulation as a reference. The same analysis is shown for the human chaperone Atox1 in its holo form (Atox1c), on the basis of previously published simulation data (*24*). Red and blue indicate negative and positive potentials, respectively.

is proportional to the solvent-accessible surface area that becomes buried upon heterocomplex formation. The WD4 heterocomplex has the highest nonpolar solvation energy contribution (Table 4) and is evidenced in the surface rendering of the complex (Figure 11A).

The energy contributions to the calculated ΔG are the result of a number of specific intermolecular contacts between holo-Atox1 and the WDs that form the interaction interface. In the Atox1−WD4 heterocomplex, an extensive and stable electrostatic network of interactions keeps the active sites in close contact (Figure 11B). Thr11 in Atox1 forms an intermolecular HB with Thr13 in WD4 (residues X_1 of the conserved motif), whereas Lys60 in Atox1 (which aligns with Phe66 of the WDs in the α2−β4 loop) forms a HB with Thr13 and Cys17 (second Cys) in WD4. At the same time, Thr13 in WD4 donates a HB to Cys15 (second Cys) in Atox1. Away from the active sites, interactions between helices α1 and α2 and the α2−β4 loop also contribute to the binding interface (Figure 11C). Gly59 in Atox1 α2−β4 loop interacts with Ser16 (residue X_3 of the conserved motif) and Ser20 in WD4 helix α1. Also, Met64 in WD4 helix α2 (only present in WD1, WD2, and WD4; Figure 1) interacts with Lys57 and Thr58 backbones in Atox1 helix α2. Finally, three intermolecular salt bridges stabilize the heterocomplex (Figure 11C): Lys57 in Atox1 with Asp63 in WD4 helix α2 (conserved among the WDs, except in WD3 and replaced by Glu in WD6; Figure 1), Arg21 in Atox1 helix α1 with Glu67 in WD4 strand β4 (present in WD1, WD2, WD4, and WD5; Figure 1), and Lys25 in Atox1 helix α1 with Glu62 (only present in WD3, WD4, and WD6; Figure 1) in WD4 helix α2.

In WD2, WD5, and WD6 heterocomplexes, the active sites interact in a similar way to WD4, whereas in WD1, the active sites are further apart. In WD2 and WD5, similar salt bridges stabilize the Atox1−WD heterocomplexes. In WD1 and WD6, however, only two of them are present. On the other hand, the Atox1−WD3 heterocomplex is weak; before the heterocomplex falls apart, the proteins make only a few intermolecular vdW contacts and a single salt bridge.

DISCUSSION

Nature's reason for the presence of six similar MBDs in ATP7A and ATP7B has been the subject of intense investigations. Solution structures of individual MBDs have shown that they all have a similar fold, which also matches that of the partner chaperone Atox1. Nonetheless, genetic and biochemical data (*28*−*30*) imply that the six WD domains (and also the six MBDs in ATP7A) are not functionally equivalent, and possible roles include fine-tuning and regulation of the Cu transfer activity. Reported experimental data vary, likely because of the use of different constructs and experimental conditions. In Cu-chelator competition experiments using a six-domain WD construct, the affinity for Cu−Atox1 of individual Cu sites appeared similar and delivery could occur to all domains (*27*). In contrast, Cys-labeling studies have suggested that, in the full N-terminal domain, Cu−Atox1 preferentially delivers the metal to WD2 (*23*). On the other hand, NMR experiments showed that Atox1 can form a Cu-dependent adduct with both WD2 and WD4 when presented as individual domains (*17*) and Cu−Atox1

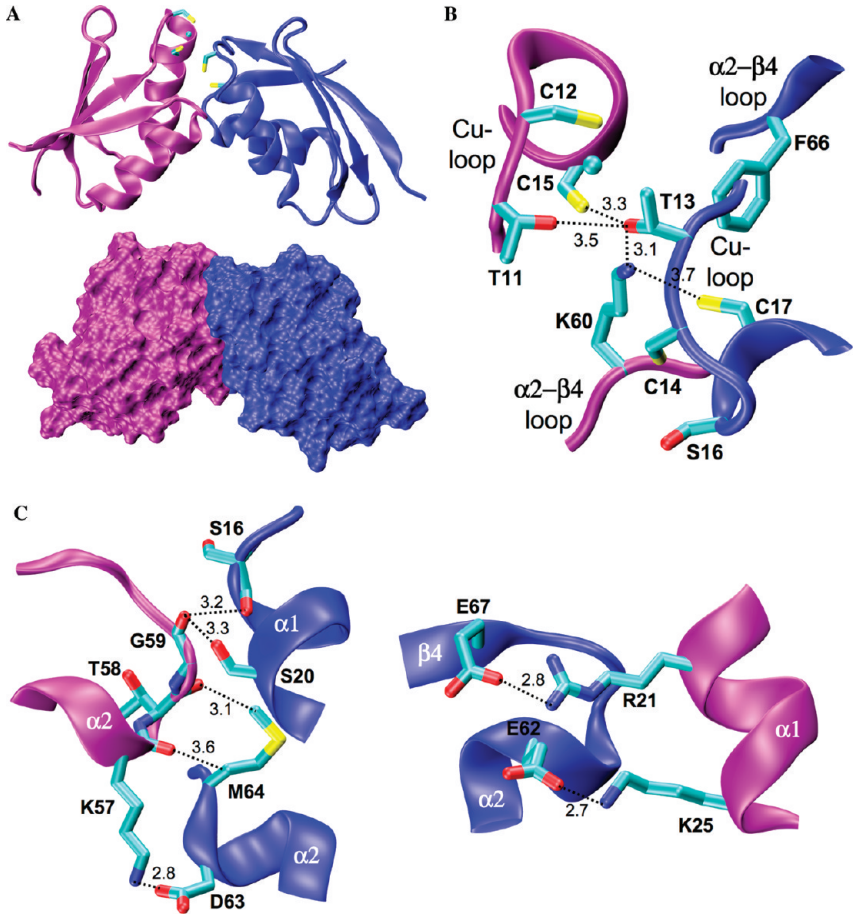

FIGURE 11: Holo-Atox1−WD4 heterocomplex. (A) Final structure after ~35 ns of MD simulation; the Cu atom and residues C_1 and C_2 from the conserved $MX_1C_1X_2X_3C_2$ motif for each protein are also shown (top). Surface representation of the final structure (bottom). (B) Zoom in of holo-Atox1 and WD4 active sites (Cu and α2−β4 loops) showing key intermolecular interactions. (C) Intermolecular interactions between helices α1, α2, and the α2−β4 loop. In all cases, holo-Atox1 is in purple and WD4 in blue.

Table 4: Free Energy (Δ*G*, kcal/mol) of Holo-Atox1−WD Heterocomplex Formation and Its Different Contributions: Intermolecular van der Waals Interactions (vdW, kcal/mol), Intermolecular Coulomb Interactions (Electrostatic, kcal/mol), Change in Reaction Field Energy (Reaction Field, kcal/mol), and Nonpolar Solvation Energy (Cavity, kcal/mol)[a]

	Δ*G*	vdW	electrostatic	reaction field	cavity
Atox1c−WD1	−8.1 ± 0.6	−47 ± 5	−74 ± 11	79 ± 10	−8.4 ± 0.6
Atox1c−WD2	−8.2 ± 0.7	−48 ± 6	−99 ± 11	106 ± 9	−9.0 ± 0.6
Atox1c−WD3	−4.2 ± 0.6	−12 ± 5	−38 ± 12	40 ± 11	−2 ± 1
Atox1c−WD4	−9.5 ± 0.4	−50 ± 4	−172 ± 12	169 ± 10	−9.7 ± 0.4
Atox1c−WD5	−9.1 ± 0.5	−50 ± 5	−120 ± 11	119 ± 9	−9.4 ± 0.8
Atox1c−WD6	−8.0 ± 0.5	−45 ± 4	−50 ± 9	54 ± 8	−8.5 ± 0.7

[a] Reported energy values correspond to the average of 100 calculations based on the last 10 ns of MD simulations of each heterocomplex. Errors correspond to the standard deviation.

preferentially delivered Cu to WD4 in a WD34 construct via the formation of an Atox1−Cu−WD4 adduct (*16*). Similar NMR experiments on a WD56 construct revealed that Atox1 did not interact with these domains but that, instead, Cu-loaded WD4 could interact with WD6 in the WD56 construct and form a Cu-dependent heterocomplex (*17*). Subsequent NMR experiments from this year involved a construct with all six WD domains present: the new data suggest that, at these conditions, WD domains 1, 2, and 4 formed adducts with Cu−Atox1 but the remaining domains, although metalated by Atox1, did not form detectable adducts (*52*). Using two-hybrid assays, it has been reported that combinations of WD1−WD4 but not WD5 and WD6 interacted with Atox1 (*31*−*33*). In one such study, preferential interactions between Atox1 and WD4 were demonstrated, although, in addition to the dominant Atox1 interaction with WD4, Atox1 was found to interact also with WD1 and WD2 (*33*). When taken together, it appears that all WD domains have an ability to interact with Atox1 but that kinetic and thermodynamic properties (perhaps governed by intrinsic domain properties, interdomain interactions, and the surrounding media) will act as selectivity filters at limiting conditions.

To address the role of intrinsic biophysical properties of individual domains, we here compared the *in silico* behavior of the six MBDs of ATP7B. We hypothesized that selective Cu delivery by Atox1 to MBDs in ATP7B is governed by differential conformational flexibility and/or Cys solvent exposure among the WDs. For example, one may propose that some domains are more poised than others to form partially folded intermediates that are involved in heterocomplex formation. We have previously determined that holo-Atox1 is a rigid and stable protein in comparison to the bacterial Cu chaperone CopZ (*24*, *53*). It is tempting to speculate that, because of this, Atox1 will form more stable complexes with WD domains that are more floppy and can adapt. Moreover, we recently reported data that suggests that key residues near or in the Cu loop have evolved differently in Cu chaperones from different species to allow for fine tuning of the flexibility of the loop (*54*, *55*).

As predicted, our simulations demonstrate that the individual WDs are not equivalent at the molecular level. First, because of the presence of a unique Pro, WD3 behaves differently from the rest: the Cu loop is rigid (and adopts a different conformation than in the other domains), whereas the overall fold is more floppy. WD5 is also an outlier because its final structure is different from the starting structure and helix α1 becomes distorted. WD1, WD2, and WD6 display many similar trends: their folds are stable, and their Cu loops are more well-defined than in WD4 and WD5. Of all the domains, WD6 is the least flexible when comparing rmsd and rmsf data. WD4 retains the starting structure, but it is very dynamic during the simulation. In WD4, helix α1 completely unwinds and rewinds during the simulation, whereas this helix only partially unwinds in WD1, WD2, and WD6. No helix α1 unwinding motion is found in WD3 or WD5 domains. Therefore, we propose that unwinding of helix α1 may be important for recognition of partner proteins during Cu transfer, such as Atox1 in the case of WD1, WD2, and WD4, and interdomain recognition (by WD4 for example) in the case of WD6. The Cys−Cys distance in the different WD domains also vary: from short (in WD1, WD2, WD5, and WD6) to intermediate (in WD4) to long (in WD3). In addition, subtle differences among the domains in the interaction network around the Cu site and the α2−β4 loop, regions believed to be involved in heterocomplex formation, have been noted. The many experimental implications of favorable Atox1 interactions with WD4 (see above) can thus be explained by a requirement of helix α1 unwinding to form a stable complex with Atox1. Cys1, which is proposed to be the first Cys to bind Cu during transfer (*56*), is most exposed in WD4, and the Cys−Cys distance distribution in WD4 is similar to that found in apo-Atox1. These features may also serve as a selectivity filter for specific Cu−Atox1 recognition with WD4.

Inspection of the electrostatic surface potentials predicts favorable interactions between holo-Atox1 and both WD2 and WD4, as also noted experimentally (*17*, *23*, *33*, *52*). Moreover, the WD4 surface becomes more negative upon Cu binding, especially on the Cu loop, which complements the positive patches in apo-WD6 and not the negative ones in apo-WD5. Electrostatic attraction may thus explain why WD4c preferentially delivers the metal to WD6 in a WD56 construct (*17*). In addition, we found that WD4c is the most flexible of all holo domains simulated here and its Cu site protrudes from the surface of the protein. It is possible that the unique flexibility of WD4c is a good match for the interaction with WD6, which is the most rigid WD domain (when comparing apo forms), as also observed experimentally (*17*).

From additional simulations on two ATP7A domains, MK1 and MK2 (data not shown), we can use similar arguments (i.e., importance of domain dynamics and complementary electrostatic surfaces) to predict that MK1 would be favored over MK2 for the Cu−Atox1 interaction. We have found that both MK1 and MK2 exhibit significant backbone dynamics and the Cu loop is floppy (much like WD4); however, whereas MK2 has mainly positive patches on the predicted Atox1 interaction surface, MK1 has a negative such surface. In agreement, a preferential Atox1 interaction with MK1 over MK2 has been observed in experiments (*34*, *57*).

We note that our simulations for WD3−WD6 start from NMR solution structures obtained with two-domain constructs; thus, it is reasonable that the final structures in our simulations divert from the initial NMR data. We have performed similar MD simulations on WD34 and WD56 two-domain constructs (data not shown). We found that, in both cases, covalent attachment affects the structure and dynamics of the individual domains, although at different extents. This is expected in the case of WD56, in which the NMR structure revealed tight packing between the two domains (*17*). Both WD5 and WD6 structures differ less from the initial NMR structure when covalently attached than when individually simulated. In particular, WD5 fluctuations are significantly reduced in the two-domain construct compared to the isolated domain ($rmsd_{100}$ of 0.8 ± 0.1 versus 1.3 ± 0.4 Å). On the other hand, the NMR structure of the WD34 construct shows no significant domain−domain interactions (*16*). However, the construct used for NMR consists of several segments that are lacking in the individual domains: a N-terminal 17-residue linker (before WD3), a 27-residue linker that connects domains 3 and 4, and a C-terminal 11-residue linker (after WD4). We observed significant interactions between these linkers and the individual domains throughout the simulations, suggesting that covalent attachment also affects domain dynamics in WD34.

Simulations of the six different Atox1−WD heterocomplexes provide insights into the nature and strength of intermolecular interactions. We found that, from the six WDs, WD4 binds most strongly to holo-Atox1, with the electrostatic interactions having the greatest contribution. This was expected on the basis of the surface electrostatic potential of the individual domains, which predicted that the complementary charge surface would be maximized in the Atox1−WD4 heterocomplex. Although the Atox1−WD2 heterocomplex is also energetically favorable, we found a difference of ∼1.3 kcal/mol in favor of the WD4 complex, which explains why, when presented as individual domains *in vitro*, WD4 interacts stronger than WD2 with holo-Atox1 (*17*). Holo-Atox1 forms an heterocomplex with WD1 with similar Δ*G* than the one formed with WD2, which explains their interaction *in vitro* (*52*). On the other hand, WD3 and WD6 heterocomplexes have the weakest intermolecular vdW and electrostatic interactions, indicating that complexes between these domains and holo-Atox1 are not as energetically favorable as the rest of the domains. WD3 binds very poorly to holo-Atox1, with a difference in Δ*G* of over 5 kcal/mol as compared to the strongest Atox1 binder, WD4. This explains why holo-Atox1 preferentially delivered Cu to WD4 in a WD34 construct *in vitro* (*16*). To note, electrostatic interactions appear to play an important role in Atox1−WD adduct formation. These interactions are the component of Δ*G* that varies the most among the six heterocomplexes and strongly correlate with the stability of the heterocomplexes (Table 4).

As predicted, the most flexible domains, WD4 and WD5, form the most stable heterocomplexes with the rigid chaperone holo-Atox1. However, no chaperone−target adduct formation was detected *in vitro* for WD5 (*17*, *52*). We propose three possible explanations for this discrepancy. First, we are studying the binding of individual domains to Atox1, as opposed to experiments in which two-domain (*17*) or six-domain (*52*) constructs were used. As explained above, the presence of other domains may affect the dynamics and structure of the isolated domain. In fact, whereas the flexibility of WD5 is significantly reduced in the WD56 construct, WD4 is still flexible in the WD34 construct (data not shown). Thus, backbone rigidity (in a two-domain construct) and/or its relative location in the full N terminus of ATP7B (in a six-domain construct) may explain the lack of detectable interactions between WD5 and Atox1 *in vitro*.

Second, our analysis is based on the already formed chaperone−target adduct and does not take into account the kinetic barrier of complex formation. Third, our classical MD simulations do not allow for Cu^I transfer between Atox1 and the WD; the kinetic of the transfer reaction and relative stability of its intermediates may affect the heterocomplex stability and its detection *in vitro*.

Several missense mutations found in Wilson disease patients have been located in the WD domains: G85V (*58*), L492S (*58*), Y532H (*59*), G591D (*59*), A604P (*59*), R616W (*60*), and G626A (*61*). Inspection of the behaviors of residues Gly85 (Gly30 in WD1), Leu492, and Tyr532 (Leu8 and Tyr48, respectively, in WD5) and Gly591, Ala604, Arg616, and Gly626 (Gly28, Ala41, Arg53, and Gly63, respectively, in WD6) during the simulations, may reveal why and how mutations at these positions cause disease. Gly30/28 in WD1/6 is located in the α1−β2 loop and is completely conserved among all of the WDs (Figure 1). Mutation of this small residue to a larger one, such as Val or Asp, will likely be detrimental to the fold, because there is no space for a bulkier side chain. Leu8 in WD5 is located in strand β1 and is conserved as a hydrophobic residue among the WDs (Figure 1). Throughout the entire simulation, Leu8 forms an extensive network of hydrophobic interactions with residues in helix α2 (Ile58, Ala59, and Ile62): mutation of this position to a polar residue (such as Ser as in the disease variant) will likely reduce the stability of the core. Tyr48 is located at the end of strand β3 in WD5 and is also conserved among the WDs, replaced by a Phe only in WD6 (Figure 1). During the simulation, its aromatic ring forms a stable interaction with the conserved Pro50 and Pro55 in the β3−α2 loop and helix α2, respectively, stabilizing this loop. Mutation to a polar His (as found in a disease variant) will likely perturb these interactions. Ala41 is located in strand β3 in WD6: it is conserved among all of the WDs (Figure 1) and interacts in the protein core. Mutation of this residue to a Pro (as found in a disease variant) will probably disrupt the conformation of this β strand. Arg53 is located in helix α2 in WD6 and is facing the protein surface. This residue may therefore be involved in interdomain interactions. Gly63 in WD6 is conserved in all WDs but WD3 (Figure 1), and it is located in the α2−β4 loop, one residue upstream of the conserved Phe, and thus in the region for domain−domain interactions. Changing this small side chain may reduce or alter loop dynamics and thereby affect adduct formation. When taken together, we can predict that many disease-causing mutations will result in domain unfolding/instability but some may instead disturb protein−protein interactions. Although WD5 is not found to be of particular importance in Atox1 interactions or in interdomain interactions, destabilizing mutations in this domain can cause Wilson disease: this clearly implies that the domains affect each other, directly or via the linkers *in vivo*. Finally, analysis of the WD56 two-domain construct simulation (data not shown) shows similar roles for the aforementioned residues. Arg53 in WD6, which faces the protein surface, interacts with Phe7 and Glu45 located in strands β1 and β3 of WD5, respectively, during more than 70% of our production MD simulations. This residue is therefore key for domain−domain interactions (as proposed above based on simulation of the individual domain). Mutation of this Arg to a Trp (as found in a disease variant) will disrupt a strong electrostatic interaction between WD5 and WD6, which may be relevant *in vivo*.

In summary, our computational data on the WD domains provides many structural and dynamic details (that cannot easily be obtained via experiments) that can be used as a basis for interpretation and explanation of experimental *in vivo* and *in vitro* data on the Cu transfer proteins. We note that this study is one piece in a big puzzle: the next step will be to simulate each domain covalently connected to its neighbor via the natural linker. On the basis of the *in silico* properties found for individual WDs as well as Atox1−WD heterocomplexes, we propose that (a) overall fold and Cu-loop dynamics (floppy favoring Atox1 interaction), (b) Cys−Cys distance and positioning (rather long distance and solvent exposure favor Atox1 interaction), (c) helix α1 conformation (unwinding/rewinding motion favors Atox1 interaction), and (d) electrostatic attraction are properties that vary distinctly among the six WD domains and can act as selectivity filters to guide Atox1 interactions and interdomain Cu transfer. Other factors, such as the quaternary structure of the full-length six-domain segment and the surrounding environment may further limit these reactions *in vivo*.

ACKNOWLEDGMENT

We thank Drs. Bertini and Banci for providing the PDB structure of WD34 before publication.

REFERENCES

(1) Bertinato, J., and L'Abbe, M. R. (2004) Maintaining copper homeostasis: Regulation of copper-trafficking proteins in response to copper deficiency or overload. *J. Nutr. Biochem. 15*, 316–322.
(2) Lutsenko, S., Barnes, N. L., Bartee, M. Y., and Dmitriev, O. Y. (2007) Function and regulation of human copper-transporting ATPases. *Physiol. Rev. 87*, 1011–1046.
(3) Rae, T. D., Schmidt, P. J., Pufahl, R. A., Culotta, V. C., and O'Halloran, T. V. (1999) Undetectable intracellular free copper: The requirement of a copper chaperone for superoxide dismutase. *Science 284*, 805–808.
(4) Pufahl, R. A., Singer, C. P., Peariso, K. L., Lin, S. J., Schmidt, P. J., Fahrni, C. J., Culotta, V. C., Penner-Hahn, J. E., and O'Halloran, T. V. (1997) Metal ion chaperone function of the soluble Cu(I) receptor Atx1. *Science 278*, 853–856.
(5) Klomp, L. W., Lin, S. J., Yuan, D. S., Klausner, R. D., Culotta, V. C., and Gitlin, J. D. (1997) Identification and functional expression of HAH1, a novel human gene involved in copper homeostasis. *J. Biol. Chem. 272*, 9221–9226.
(6) Hung, I. H., Casareno, R. L., Labesse, G., Mathews, F. S., and Gitlin, J. D. (1998) HAH1 is a copper-binding protein with distinct amino acid residues mediating copper homeostasis and antioxidant defense. *J. Biol. Chem. 273*, 1749–1754.
(7) Bull, P. C., and Cox, D. W. (1994) Wilson disease and Menkes disease: New handles on heavy-metal transport. *Trends Genet. 10*, 246–252.
(8) Terada, K., Schilsky, M. L., Miura, N., and Sugiyama, T. (1998) ATP7B (WND) protein. *Int. J. Biochem. Cell Biol. 30*, 1063–1067.
(9) Arguello, J. M., Eren, E., and Gonzalez-Guerrero, M. (2007) The structure and function of heavy metal transport P1B−ATPases. *Biometals 20*, 233–248.
(10) Gitschier, J., Moffat, B., Reilly, D., Wood, W. I., and Fairbrother, W. J. (1998) Solution structure of the fourth metal-binding domain from the Menkes copper-transporting ATPase. *Nat. Struct. Biol. 5*, 47–54.
(11) Banci, L., Bertini, I., Del Conte, R., D'Onofrio, M., and Rosato, A. (2004) Solution structure and backbone dynamics of the Cu(I) and apo forms of the second metal-binding domain of the Menkes protein ATP7A. *Biochemistry 43*, 3396–3403.
(12) Banci, L., Bertini, I., Cantini, F., Chasapis, C. T., Hadjiliadis, N., and Rosato, A. (2005) A NMR study of the interaction of a three-domain construct of ATP7A with copper(I) and copper(I)−HAH1: The interplay of domains. *J. Biol. Chem. 280*, 38259–38263.
(13) Banci, L., Bertini, I., Cantini, F., Migliardi, M., Rosato, A., and Wang, S. (2005) An atomic-level investigation of the disease-causing A629P mutant of the Menkes protein, ATP7A. *J. Mol. Biol. 352*, 409–417.
(14) DeSilva, T. M., Veglia, G., and Opella, S. J. (2005) Solution structures of the reduced and Cu(I) bound forms of the first metal binding sequence of ATP7A associated with Menkes disease. *Proteins 61*, 1038–1049.

(15) Banci, L., Bertini, I., Cantini, F., DellaMalva, N., Herrmann, T., Rosato, A., and Wuthrich, K. (2006) Solution structure and intermolecular interactions of the third metal-binding domain of ATP7A, the Menkes disease protein. *J. Biol. Chem. 281*, 29141–29147.

(16) Banci, L., Bertini, I., Cantini, F., Rosenzweig, A. C., and Yatsunyk, L. A. (2008) Metal binding domains 3 and 4 of the Wilson disease protein: Solution structure and interaction with the copper(I) chaperone HAH1. *Biochemistry 47*, 7423–7429.

(17) Achila, D., Banci, L., Bertini, I., Bunce, J., Ciofi-Baffoni, S., and Huffman, D. L. (2006) Structure of human Wilson protein domains 5 and 6 and their interplay with domain 4 and the copper chaperone HAH1 in copper uptake. *Proc. Natl. Acad. Sci. U.S.A. 103*, 5729–5734.

(18) DiDonato, M., Narindrasorasak, S., Forbes, J. R., Cox, D. W., and Sarkar, B. (1997) Expression, purification, and metal binding properties of the N-terminal domain from the wilson disease putative copper-transporting ATPase (ATP7B). *J. Biol. Chem. 272*, 33279–33282.

(19) Lutsenko, S., Petrukhin, K., Cooper, M. J., Gilliam, C. T., and Kaplan, J. H. (1997) N-Terminal domains of human copper-transporting adenosine triphosphatases (the Wilson's and Menkes disease proteins) bind copper selectively in vivo and in vitro with stoichiometry of one copper per metal-binding repeat. *J. Biol. Chem. 272*, 18939–18944.

(20) Ralle, M., Cooper, M. J., Lutsenko, S., and Blackburn, N. J. (1998) The Menkes disease protein binds copper via novel 2-coordinate Cu (I)-cysteinates in the N-terminal domain. *J. Am. Chem. Soc. 120*, 13525–13526.

(21) Arnesano, F., Banci, L., Bertini, I., Ciofi-Baffoni, S., Molteni, E., Huffman, D. L., and O'Halloran, T. V. (2002) Metallochaperones and metal-transporting ATPases: A comparative analysis of sequences and structures. *Genome Res. 12*, 255–271.

(22) Ralle, M., Lutsenko, S., and Blackburn, N. J. (2004) Copper transfer to the N-terminal domain of the Wilson disease protein (ATP7B): X-ray absorption spectroscopy of reconstituted and chaperone-loaded metal binding domains and their interaction with exogenous ligands. *J. Inorg. Biochem. 98*, 765–774.

(23) Walker, J. M., Huster, D., Ralle, M., Morgan, C. T., Blackburn, N. J., and Lutsenko, S. (2004) The N-terminal metal-binding site 2 of the Wilson's disease protein plays a key role in the transfer of copper from Atox1. *J. Biol. Chem. 279*, 15376–15384.

(24) Rodriguez-Granillo, A., and Wittung-Stafshede, P. (2008) Structure and dynamics of Cu(I) binding in copper chaperones Atox1 and CopZ: A computer simulation study. *J. Phys. Chem. 112*, 4583–4593.

(25) Cobine, P. A., George, G. N., Winzor, D. J., Harrison, M. D., Mogahaddas, S., and Dameron, C. T. (2000) Stoichiometry of complex formation between copper(I) and the N-terminal domain of the Menkes protein. *Biochemistry 39*, 6857–6863.

(26) Wernimont, A. K., Yatsunyk, L. A., and Rosenzweig, A. C. (2004) Binding of copper(I) by the Wilson disease protein and its copper chaperone. *J. Biol. Chem. 279*, 12269–12276.

(27) Yatsunyk, L. A., and Rosenzweig, A. C. (2007) Cu(I) binding and transfer by the N terminus of the Wilson disease protein. *J. Biol. Chem. 282*, 8622–8631.

(28) Iida, M., Terada, K., Sambongi, Y., Wakabayashi, T., Miura, N., Koyama, K., Futai, M., and Sugiyama, T. (1998) Analysis of functional domains of Wilson disease protein (ATP7B) in *Saccharomyces cerevisiae*. *FEBS Lett. 428*, 281–285.

(29) Strausak, D., La Fontaine, S., Hill, J., Firth, S. D., Lockhart, P. J., and Mercer, J. F. (1999) The role of GMXCXXC metal binding sites in the copper-induced redistribution of the Menkes protein. *J. Biol. Chem. 274*, 11170–11177.

(30) Cater, M. A., Forbes, J., La Fontaine, S., Cox, D., and Mercer, J. F. (2004) Intracellular trafficking of the human Wilson protein: The role of the six N-terminal metal-binding sites. *Biochem. J. 380*, 805–813.

(31) Larin, D., Mekios, C., Das, K., Ross, B., Yang, A. S., and Gilliam, T. C. (1999) Characterization of the interaction between the Wilson and Menkes disease proteins and the cytoplasmic copper chaperone, HAH1p. *J. Biol. Chem. 274*, 28497–28504.

(32) Strausak, D., Howie, M. K., Firth, S. D., Schlicksupp, A., Pipkorn, R., Multhaup, G., and Mercer, J. F. (2003) Kinetic analysis of the interaction of the copper chaperone Atox1 with the metal binding sites of the Menkes protein. *J. Biol. Chem. 278*, 20821–20827.

(33) van Dongen, E. M., Klomp, L. W., and Merkx, M. (2004) Copper-dependent protein−protein interactions studied by yeast two-hybrid analysis. *Biochem. Biophys. Res. Commun. 323*, 789–795.

(34) Banci, L., Bertini, I., Cantini, F., Della-Malva, N., Migliardi, M., and Rosato, A. (2007) The different intermolecular interactions of the soluble copper-binding domains of the menkes protein, ATP7A. *J. Biol. Chem. 282*, 23140–23146.

(35) Eswar, N., Webb, B., Marti-Renom, M. A., Madhusudhan, M. S., Eramian, D., Shen, M. Y., Pieper, U., and Sali, A. (2007) Comparative protein structure modeling using MODELLER, Curr. Protoc. Protein Sci. Chapter 2, Unit 2 9.

(36) Wernimont, A. K., Huffman, D. L., Lamb, A. L., O'Halloran, T. V., and Rosenzweig, A. C. (2000) Structural basis for copper transfer by the metallochaperone for the Menkes/Wilson disease proteins. *Nat. Struct. Biol. 7*, 766–771.

(37) Case, D. A., Darden, T. A., Cheatham, T. E., III, Simmerling, C. L., Wang, J., Duke, R. E., Luo, R., Merz, K. M., Pearlman, D. A., Crowley, M., Walker, R. C., Zhang, W., Wang, B., Hayik, S., Roitberg, A., Seabra, G., Wong, K. F., Paesani, F., Wu, X., Brozell, S., Tsui, V., Gohlke, H., Yang, L., Tan, C., Mongan, J., Hornak, V., Cui, G., Beroza, P., Mathews, D. H., Schafmeister, C., Ross, W. S., and Kollman, P. A. (2006) AMBER 9, University of California, San Francisco, CA.

(38) Jorgensen, W. L., Chandrasekhar, J., Madura, J., Impey, R. W., and Klein, M. L. (1983) Comparison of simple potential functions for simulating liquid water. *J. Chem. Phys. 79*, 926–935.

(39) Hornak, V., Abel, R., Okur, A., Strockbine, B., Roitberg, A., and Simmerling, C. (2006) Comparison of multiple Amber force fields and development of improved protein backbone parameters. *Proteins 65*, 712–725.

(40) Berendsen, H. J., Postma, J. P., van Gunsteren, W. F., Di Nola, A., and Haak, J. R. (1984) Molecular dynamics with coupling to an external bath. *J. Chem. Phys. 81*, 3684–3690.

(41) Ryckaert, J. P., Ciccotti, G., and Berendsen, H. J. C. (1977) Numerical-integration of Cartesian equations of motion of a system with constraints: Molecular dynamics of *N*-alkanes. *J. Comput. Phys. 23*, 327–341.

(42) Baker, N. A., Sept, D., Joseph, S., Holst, M. J., and McCammon, J. A. (2001) Electrostatics of nanosystems: Application to microtubules and the ribosome. *Proc. Natl. Acad. Sci. U.S.A. 98*, 10037–10041.

(43) Crespo, A., Scherlis, D. A., Marti, M. A., Ordejón, P., Roitberg, A. E., and Estrin, D. A. (2003) A DFT based QM−MM approach designed for the treatment of large molecular systems: Application to chorismate mutase. *J. Phys. Chem. B 107*, 13728–13736.

(44) Soler, J. M., Artacho, E., Gale, J. D., Garcia, A., Junquera, J., Ordejon, P., and Sanchez-Portal, D. (2002) The SIESTA method for ab initio order-N materials simulation. *J. Phys.: Condens. Matter 14*, 2745–2779.

(45) Crespo, A., Marti, M. A., Roitberg, A. E., Amzel, L. M., and Estrin, D. A. (2006) The catalytic mechanism of peptidylglycine α-hydroxylating monooxygenase investigated by computer simulation. *J. Am. Chem. Soc. 128*, 12817–12828.

(46) Perdew, J. P., Burke, K., and Ernzerhof, M. (1996) Generalized gradient approximation made simple. *Phys. Rev. Lett. 77*, 3865–3868.

(47) Bayly, C. I., Cieplak, P., Cornell, W. D., and Kollman, P. A. (1993) A well-behaved electrostatic potential based method using charge restraints for deriving atomic charges—The RESP model. *J. Phys. Chem. 97*, 10269–10280.

(48) Frisch, M. J., Trucks, G. W., Schlegel, H. B., Scuseria, G. E., Robb, M. A., Cheeseman, J. R., Montgomery, J. A., Jr., Vreven, T., Kudin, K. N., Burant, J. C., Millam, J. M., Iyengar, S. S., Tomasi, J., Barone, V., Mennucci, B., Cossi, M., Scalmani, G., Rega, N., Petersson, G. A., Nakatsuji, H., Hada, M., Ehara, M., Toyota, K., Fukuda, R., Hasegawa, J., Ishida, M., Nakajima, T., Honda, Y., Kitao, O., Nakai, H., Klene, M., Li, X., Knox, J. E., Hratchian, H. P., Cross, J. B., Bakken, V., Adamo, C., Jaramillo, J., Gomperts, R., Stratmann, R. E., Yazyev, O., Austin, A. J., Cammi, R., Pomelli, C., Ochterski, J. W., Ayala, P. Y., Morokuma, K., Voth, G. A., Salvador, P., Dannenberg, J. J., Zakrzewski, V. G., Dapprich, S., Daniels, A. D., Strain, M. C., Farkas, O., Malick, D. K., Rabuck, A. D., Raghavachari, K., Foresman, J. B., Ortiz, J. V., Cui, Q., Baboul, A. G., Clifford, S., Cioslowski, J., Stefanov, B. B., Liu, G., Liashenko, A., Piskorz, P., Komaromi, I., Martin, R. L., Fox, D. J., Keith, T., Al-Laham, M. A., Peng, C. Y., Nanayakkara, A., Challacombe, M., Gill, P. M. W., Johnson, B., Chen, W., Wong, M. W., Gonzalez, C., and Pople, J. A. (2004) Gaussian 03, Revision D.01, Gaussian, Inc., Wallingford, CT.

(49) Holt, B. T., and Merz, K. M. Jr. (2007) Insights into Cu(I) exchange in HAH1 using quantum mechanical and molecular simulations. *Biochemistry 46*, 8816–8826.

(50) Dalosto, S. D. (2007) Computer simulation of the interaction of Cu (I) with cys residues at the binding site of the yeast metallochaperone Cu(I)−Atx1. *J. Phys. Chem. 111*, 2932–2940.

(51) Naim, M., Bhat, S., Rankin, K. N., Dennis, S., Chowdhury, S. F., Siddiqi, I., Drabik, P., Sulea, T., Bayly, C. I., Jakalian, A., and Purisima, E. O. (2007) Solvated interaction energy (SIE) for scoring protein−ligand binding affinities. 1. Exploring the parameter space. *J. Chem. Inf. Model. 47*, 122–133.
(52) Banci, L., Bertini, I., Cantini, F., Massagni, C., Migliardi, M., and Rosato, A. (2009) An NMR study of the interaction of the N-terminal cytoplasmic tail of the Wilson disease protein with copper(I)−Hah1. *J. Biol. Chem. 284*, 9354–9360.
(53) Hussain, F., and Wittung-Stafshede, P. (2007) Impact of cofactor on stability of bacterial (CopZ) and human (Atox1) copper chaperones. *Biochim. Biophys. Acta 1774*, 1316–1322.
(54) Rodriguez-Granillo, A., and Wittung-Stafshede, P. (2009) Differential roles of Met10, Thr11, and Lys60 in structural dynamics of human copper chaperone Atox1. *Biochemistry 48*, 960–972.
(55) Rodriguez-Granillo, A., and Wittung-Stafshede, P. (2009) Tuning of copper-loop flexibility in *Bacillus subtilis* CopZ copper chaperone: Role of conserved residues. *J. Phys. Chem. B 113*, 1919–1932.
(56) Banci, L., Bertini, I., Cantini, F., Felli, I. C., Gonnelli, L., Hadjiliadis, N., Pierattelli, R., Rosato, A., and Voulgaris, P. (2006) The Atx1−Ccc2 complex is a metal-mediated protein−protein interaction. *Nat. Chem. Biol. 2*, 367–368.
(57) Banci, L., Bertini, I., Ciofi-Baffoni, S., Chasapis, C. T., Hadjiliadis, N., and Rosato, A. (2005) An NMR study of the interaction between the human copper(I) chaperone and the second and fifth metal-binding domains of the Menkes protein. *FEBS J. 272*, 865–871.
(58) Loudianos, G., Dessi, V., Lovicu, M., Angius, A., Nurchi, A., Sturniolo, G. C., Marcellini, M., Zancan, L., Bragetti, P., Akar, N., Yagci, R., Vegnente, A., Cao, A., and Pirastu, M. (1998) Further delineation of the molecular pathology of Wilson disease in the Mediterranean population. *Hum. Mutat. 12*, 89–94.
(59) Cox, D. W., Prat, L., Walshe, J. M., Heathcote, J., and Gaffney, D. (2005) Twenty-four novel mutations in Wilson disease patients of predominantly European ancestry. *Hum. Mutat. 26*, 280.
(60) Caca, K., Ferenci, P., Kuhn, H. J., Polli, C., Willgerodt, H., Kunath, B., Hermann, W., Mossner, J., and Berr, F. (2001) High prevalence of the H1069Q mutation in East German patients with Wilson disease: Rapid detection of mutations by limited sequencing and phenotype−genotype analysis. *J. Hepatol. 35*, 575–581.
(61) Figus, A., Angius, A., Loudianos, G., Bertini, C., Dessi, V., Loi, A., Deiana, M., Lovicu, M., Olla, N., and Sole, G.; et al. (1995) Molecular pathology and haplotype analysis of Wilson disease in Mediterranean populations. *Am. J. Hum. Genet. 57*, 1318–1324.